Controlled Attachment of a Separated Boundary Layer in an Adverse Pressure Gradient Over a Curved Surface

C. J. Peterson[1], B. Vukasinovic[2], M. J. Smith[3] and A. Glezer[4]

Woodruff School of Mechanical Engineering, Georgia Institute of Technology, Atlanta, GA 30332-0405, USA.

A closed separation domain that forms by the adverse pressure gradient over a nominally 2-D curved surface modeling the suction surface of an airfoil is investigated experimentally in a small-scale wind tunnel operated at an inlet Mach number $M = 0.25$. The separation is manipulated by a spanwise array of fluidic oscillating jets and the effects of the actuation on the ensuing flow structure are investigated using high-resolution stereo particle image velocimetry with specific emphasis on spanwise and streamwise evolution of vorticity concentrations and turbulent characteristics. It is shown that as the actuation level increases, the outer cross flow is drawn towards the surface along the centerline of each jet and the coupled in-plane and streamwise shear, with the upwash flow between the jets, lead to the formation of multiple, opposite sense, streamwise vorticity concentrations. The high instantaneous shear between the jets also engenders elevated turbulent production and dissipation rates and is marked by halo-like structures of time-averaged concentrations of the turbulent kinetic energy. It is remarkable that the time-averaged rendition of the multiple strands of counter rotating streamwise vortices are manifested by the organized time-averaged counter-rotating adjacent vortex pairs that stretch away from the surface as they are advected downstream within the attached flow.

Nomenclature

A_∞	=	area of test section inlet
c	=	model chord length
C_μ	=	momentum coefficient
H	=	test section height
M	=	Mach number
ρ_∞	=	density of air at test section inlet
U	=	streamwise velocity
V	=	vertical (in-plane) velocity component
V_∞	=	velocity at test section inlet
ξ_x	=	streamwise vorticity along the x-direction
ξ_y	=	cross-stream vorticity in the y-direction
x	=	streamwise coordinate direction
y	=	vertical coordinate direction
z	=	spanwise coordinate direction

[1] Ph.D. Candidate, Woodruff School of Mechanical Engineering.
[2] Senior Research Engineer, Woodruff School of Mechanical Engineering.
[3] Professor, Daniel Guggenheim School of Aerospace Engineering, AIAA Fellow.
[4] Professor, Woodruff School of Mechanical Engineering, AIAA Fellow.

I. Background

Internal flows with imposed adverse pressure gradients are highly susceptible to local, sustained flow separation that can lead to flow instabilities and significant losses. Active flow control can potentially mitigate these adverse effects by delaying separation or bypassing it altogether.

The severe losses that are associated with internal flow separation have motivated numerous investigations of the fundamental aspects of these complex flows over the years in various geometries such as flow junctions (e.g., Ethier, et al. [1]), convex banks (Blanckaert [2]), backward facing steps (Papadopoulos and Otugen [3]), and curved ducts (Yang et al. [4]), to name a few. Investigations of active control of internal flow separation have received considerable attention since the 1950s. Suzuki et al. [5] considered flow separation in a two-dimensional diffuser and its control by periodic mass injection. Their reduced-order model study showed alteration of vortex formation and dynamics in the controlled flows that led to a reduction of the separation bubble albeit with negligible changes in the separation location. Studies by Amitay et al. [6] demonstrated the effectiveness of active flow control in delaying internal separation in a duct having a rectangular cross section and reported a reduction in the streamwise scale of the separation domain and concomitant increase in the volume flow rate and reduction in losses in the presence of flow actuation. In a related investigation, Kumar and Alvi [7] demonstrated the feasibility of another flow control element, a high-speed micro-jet, for suppressing flow separation at $M < 0.2$. Banaszuk et al. [8] demonstrated the application of an adaptive flow control scheme for multi-frequency flow separation control in a planar diffuser by utilization of synthetic jets. Vaccaro et al. [9] investigated mitigation of internal flow separation in a compact rectangular offset duct (up to $M \approx 0.45$) using steady blowing at the flow boundary and showed that changes in flow attachment can affect total pressure recovery and distortion in the affected flow segment.

Analysis and comparison of internal flow separation characteristics with and without flow control are also considered in the prior and present work. Simpson [10] noted that turbulent separation has a much different structure than that for attached flows. Some of the defining characteristics are that the largest turbulent stresses occur within the middle of the free shear layer due to occurrences of large-scale vortices, which have a complex effect on pressure fluctuations and the recirculation zone. Due to the complex interactions, the separation is inherently unsteady. Of further interest is the modification of the natural turbulent separation structure under the flow control. An example of control of a shear flow is studied for the flows over a backwards facing step [11,12,13]. The study by Chun and Sung [11] demonstrates that a localized forcing effect near the separation point has significant effect on the characteristics of the separated flow structure. Specifically, the vortex roll-up procedure in the shear layer is changed, which results in varying the vortex entrainment and consequently the reattachment length off of the step.

In addition to the time-invariant effects of flow control on the nominally time-averaged spatial delay (or displacement) of the separation, another important aspect of the actuation is its effect on the flow dynamics about the delayed point of separation, which can have significant impact on global flow stability. The effects of separation control on the unsteady flow features of flow separation reattachment are of particular interest. Chun and Sung [11], Yoshioka et al., [12] and Vukasinovic et al. [13] investigated control of separating flow at a fixed separation point, formed by an abrupt change in the flow boundary over a backward-facing step. Chun and Sung [11] demonstrated that acoustic forcing near the separation point had significant effect on the characteristics of the separated flow structure by altering the roll-up of the forming vortices and thereby varying entrainment and, ultimately, the reattachment length downstream of the step. Yoshioka et al. [12] showed that the effects of actuation on flow reattachment downstream of the backward-facing step increased production of the Reynolds stresses. Vukasinovic et al. [13] attributed the increased turbulent kinetic energy production and dissipation within the separated shear layer to high-frequency (dissipative) actuation at the location of separation. The changes of the dynamics in the flow due to actuation, consequently, affect the shape of the turbulent boundary layer. The shape of the turbulent boundary layer relates to where the energy bearing fluctuations and stresses are located. Marusic and Perry [14] defined two distinct types of eddies to describe the energy-containing motion within a turbulent boundary layer. These eddies can be delineated into wall bound eddies that produce finite Reynolds stresses near the wall, where others are considered wake structures and do not impact the near wall Reynolds stress. The combination of such eddies can describe all sets of turbulent boundary layer states. This postulation shows the underlying significance of outer flow features to the turbulent flow as well. Ellsberry et al. [15], noted that boundary layers maintained close to separation over extended distances give rise to nearly linear streamwise growth of integral length scales, and that the boundary layer maintained in a non-equilibrium state required different scales to collapse the velocity and turbulence intensity profiles. They further postulated that since flow approaching separation due to an adverse pressure gradient can be identified as its shear stress at the wall approaches zero, the importance of the wall region relative to the outer region is diminished. More recently, Schatzman and Thomas [16] concluded that for turbulent boundary layers exposed to adverse pressure gradients of sufficient magnitude to give rise to an inflectional mean profile, the flow is largely governed by the existence of an outer embedded shear layer. They also stated that separation is not required for the existence of the embedded shear layer, which gives rise to the ability to create a scaling parameter based off of outer flow features. The importance of such outer flow features also gives further credence to the earlier arguments of Marusic and Perry that the flow can be described by wall-bound or wake like eddies in the flow. Peterson, Vukasinovic, and Glezer [17] investigated the dynamics and characteristic structure of natural and deliberately-delayed, migrated separating flow within a severe adverse pressure gradient and concluded that, despite expected differences in the flow dynamics about local flow separation, there is an underlying similar flow structure. Moreover, it was found that arguments made about the flow being governed by an embedded shear layer [16] can be extended to not only naturally-separating flow, but also to the controlled flow separation, such is under the strong adverse pressure gradient.

Typically, discrete flow control techniques are used to generate streamwise vortices to entrain higher momentum fluid towards the surface in order to reduce or eliminate flow separation. For example, Johnston and Nishi [18] studied the use of vortex generating jets to develop longitudinal vortices similar to those of solid vortex generators to reduce stalled regions in a turbulent boundary layer. They created longitudinal vortices of varying strength and rotational direction based on the issuance angles of the jets. For sufficiently high velocity ratios, skewed jets were shown to be effective at reducing large regions of stalled turbulent separated flow, where jets pointing directly upstream proved ineffective. They also showed that counter-rotating vortex pairs induce significant spanwise variations in the boundary layer.

Fluidic oscillators, which have no moving parts and convert a pressurized air supply into an oscillating jet, are of particular interest in flow control applications. They effect a large span-wise extent due to their oscillating nature, while limiting their cross-stream penetration [19]. Studies by Osterman et al. [19] of a fluidic oscillator issued into a crossflow, show that it develops streamwise vortices outside of the boundary layer, that are then convected by the outer crossflow. They further postulate that this mechanism is similar to a vortex-generating jet, and as the vortices develop significant wall-normal and lateral velocities, may explain its effectiveness for separation control [19]. Different integrations of the flow control elements were also studied. Skewing the jets towards the crossflow [20] resulted in only one dominant vortex being evident in the time-averaged flow fields for small velocity ratios due to the asymmetry of the developed vortex pairs. Otto et al. [21] compared the effectiveness of fluidic oscillators to steady jets on the NASA hump geometry. They showed that for a given jet spacing fluidic oscillators achieved improved control authority for lower momentum, mass, and energy coefficients as compared to steady jets. It is further shown that the fluidic oscillators produce a more structured array of streamwise vortices as compared to the steady jets, which is argued to be the cause of the improved flow control authority. Several designs of fluidic oscillators driven by the feedback loop were compared on the NASA hump model by Otto et al [22] to examine the effect of the exit angle and internal geometry. Results showed that these three designs yielded different performance despite similar operation frequencies of the jets, indicating performance was not driven by frequency characteristics. They also demonstrated that the higher performing design was characterized by the creation of a spanwise array of counter-rotating vortices in the time-averaged PIV field [22]. Woszidlo, Ostermann, Schmidt have extensively studied the two-channel design and shown that the flow fields are highly dependent upon the Strouhal number, which is coincidentally tied to the velocity ratio of the jet operation (and not the scale of the oscillator itself) [23].

The installation angle of the jets is important to their overall effectiveness. Kim and Kim [24] studied the installation parameters effect on the flow control effectiveness on a ramp model. They showed that the installation of the oscillators was most sensitive to the pitch angle of the installation, and further commented that staggering the array of the fluidic oscillators reduced their overall effectiveness as compared to a constant in-line array. At the limit of the pitched jet orientation is the creation of a wall jet, that has significantly different characteristics compared to the nominal jet (or fluidic oscillator) in cross flow that has been discussed previously. A comprehensive study by Namgyal and Hall [25] discuss some of the varying characteristics and turbulent fluctuations inherent to the turbulent wall-jet. One such observation was the development of a counter-rotating vortex pair (similar to a jet in crossflow) [25]. They also noted that the streamwise, $\overline{u^2}$ fluctuations had the highest contribution to the Reynolds stresses throughout the jet due to the larger value of the averaged streamwise U velocity along the jet. Furthermore, they also noted that the Reynolds shear stress $\overline{uv}$ was much higher along the jet centerline at all measured downstream locations, and that is was a mostly positive quantity which is seen commonly in free shear layers of jets. Further studies by Matsuda, Iida, and Hayakawa [26] of a wall-jet in the absence of a crossflow showed similar development of counter-rotating vortices due to the jet. They suggest that the wall-jet develops a similar shape to that of a horseshoe-like vortex, with the legs tilting as the jet advects downstream, which in turn induces streamwise vorticity accounting for the lateral spreading of the wall-jet in the downstream direction [26]. The study by Pauley and Eaton [27] discussed the characteristics of vortex pairs embedded in a turbulent boundary layer created by vortex generators with either common flow up (away from the surface) or down (towards the surface) between the pairs of vortices. They showed that where the secondary flow is away from the wall, there was an associated thickening of the boundary layer, and also thinning where it was towards the wall. They further commented that neighboring pairs of vortices clearly effected the spreading of the vorticity in the streamwise direction but did not increase the loss of vortex circulation. Common flow up in the center of the vortices served to carry the pair of vortices away from the wall, while common flow towards the surface between them keeps them wall bound but spreading away from each other as flow progresses downstream. Furthermore, the common flow down cases were shown to have the greatest distortion of the boundary layer over a large streamwise extent (i.e. a widening area of boundary layer thinning as the flow propagates).

The present experimental study focuses on the controlled flow's interaction with a nominally separated crossflow and the ensuing reattachment in an adverse pressure gradient. Specific emphasis and interest is placed on the local attachment mechanism due to the fluidic actuation. As such, the spanwise structure of the flow and its associated fluctuations and turbulent kinetic energy are investigated with the flow downstream evolution and with varying levels of flow control.

II. Experimental Setup and Methodology

The experiments are performed in an open-return, subsonic wind tunnel that is operated in suction (M < 0.75), where the outlet temperature of the air is controlled using a low pressure drop heat exchanger. The test geometry (Figure 1) consists of a nominal inlet duct of $W \times H$ cross-section, where the channel height H = W = 127 mm, and test section length is L = 660.4 mm. The shown test section is coupled to the outlet of the tunnel facility using an adapter section (not shown) that is filled with honeycomb and a mesh screen to provide uniform inflow to the test section. A slim-profile Pitot probe is integrated into the test section at the inlet plane for characterization of the oncoming flow Mach number, which is nominally set to M = 0.25. This probe is paired with the wall static pressure in the same plane, and this measured static pressure, along with the calculated Mach number at the test section inlet, are used as reference parameters for the flow characterization. Both the total and static pressure ports at the test section inlet are measured by two *baratron* pressure transducers and sampled by a DAQ computer. A particle image velocimetry setup is utilized for flow characterization through the test section. For that purpose, the PIV laser sheet passes through an optical window opposite the test geometry and can be rotated to illuminate planes oriented either streamwise for the centerline, planar PIV or spanwise for stereoscopic PIV as is depicted schematically in Figure 1. The side walls of the test section are made of glass, and the PIV cameras are mounted on a computer-controlled *x-y-z* traversing mechanism. Planar PIV measurements are typically done in multiple, partially-overlapping fields of view along the central plane, in order to preserve fine spatial resolution over the wide measurement domain and are integrated into a composite flow field during post-processing. Each set of planar PIV measurements is taken at 200 Hz and ensemble averages are based on over 1,000 image pairs. Additionally, stereoscopic PIV is utilized to determine spanwise characteristics of the flow. The laser sheet optics and cameras are mounted simultaneously on the *x-y-z* traverse to examine multiple streamwise locations. Stereo PIV is taken at 15 Hz and ensemble averages are taken over 800 image pairs.

The test model geometry is based on a VR-12 airfoil at a 13-degree angle of attack, with a chord length of $c \approx 62.23$ mm (Figure 1), which is chosen such to impose significant adverse pressure gradient to induce flow separation. To further promote flow separation, a trip wire (d ~0.43 mm, d/c ~.007) is mounted upstream from the airfoil model surface at $x \approx$ 300mm ($x/c \approx 4.8$) downstream of the test section inlet (x = 0). The baseline geometry is built out of the three integrated segments, such that the central one can be interchanged with a module populated with the flow control elements. Flow control is effected by fluidic oscillating jets, which have already been utilized in a number of internal and external flow control applications. These jets combine the benefits of unsteady flow control due to their oscillating nature and a net addition of mass and momentum to the flow. Another important aspect of this flow control approach is in utilization of the Coanda effect along the surface of the test geometry as the jest are issued along a convex surface. In addition, their simplicity of operation and low maintenance requirements make

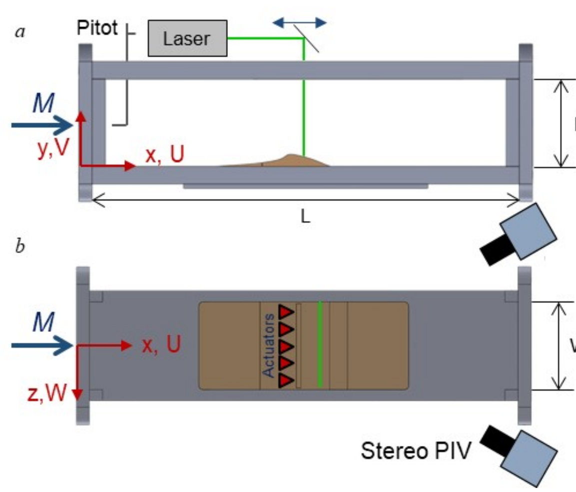

Figure 1. *Flow geometry side (a) and bottom (b) views. Stereo PIV camera locations, laser sheet alignment, and global coordinate system (x,y,z) are shown for reference.*

them suitable candidates for airborne applications. An array of 17 equally-spaced jets is deployed in the current study at a constant streamwise location x/c = 5.1 across the span of the test geometry. The jets, which orifices measure 0.5 × 1 mm on the sides, are spaced 7 mm apart. The jets nominal issuing direction is tangential to the surface moldline, while they oscillate in the spanwise direction. The jet oscillating frequency is a weak function of the fluidic oscillator flow rate and, for typical flow rates utilized in the current test, the frequency is on the order of 7-8 kHz. The flow control parameter is defined as the mass flow rate coefficient $C_\mu = Thrust_{jet}/\rho_\infty A_\infty V^2_\infty$, which is the ratio between the total momentum through the jet array and the momentum through the test section. The jet thrust is measured directly as a function of the jet flow rate during the calibration procedure on a bench-top-mounted load cell apparatus.

The spanwise PIV measurements span three full jet orifices in the center of the test section located at z/c = -0.11, 0 and 0.11. It should be noted that the y/c coordinate at different streamwise locations is defined locally, relative to the local surface elevation. This is done for convenient comparison of the local flow features in the vicinity of the surface.

III. Streamwise Vorticity Concentrations Effected by Fluidic Actuation

The primary interest of the present study is the interaction of the control jets with a separated crossflow. For that purpose, particle image velocimetry is the primary tool for investigating the flow fields along the jets' streamwise issuance paths. Several spanwise, high-resolution PIV fields of view are measured along the flow evolution to examine the streamwise flow features, as well as their downstream evolution. Prior experimental work [28] focused on examining the global flow features within the center plane, as well as the local separation and reattachment characteristics. To illustrate this global flow evolution, two planar composite flow fields at M = 0.25 are shown in Figure 2 as equidistant mean velocity vectors overlaid over raster plots of the mean spanwise vorticity, and of the associated turbulent kinetic energy (TKE), for the unactuated flow (Figure 2a, b) and the flow actuated with $C_\mu \cdot 10^3 = 2.1$ (Figure 2c, d). The unactuated flow's mean recirculating bubble is fully captured in this composite view and it is bound by a large separated shear layer which originates off the aft side of the surface at $x/c \approx 5.2$. As the separated shear layer grows in the flow direction, marked by diffusion of the initially concentrated vorticity layer, it begins to deflect back toward the surface at the end of the geometrically imposed adverse pressure gradient and eventually reattaches at $x/c \approx 6.4$. The TKE contained within the field of view peaks downstream of the separation, arguably due to the formation of larger scale structures in the growing shear layer, before the flow reattaches (Figure 2b). It has been shown [28] that increased levels of C_μ progressively delay the flow separation and reduce the recirculating domain; the actuation level shown (Figure 2c, d) is sufficient to keep the flow attached within the measurement domain. Along with the prolonged flow attachment with C_μ, the vorticity layer becomes increasingly wall bound, which also impedes the flow mixing and limits the shear layer growth. It is interesting to note that even when the flow remains fully attached throughout the aft flow domain, there is still a remnant of wall-bound vorticity, as seen in Figure 2c. Additionally, the peak TKE levels are significantly reduced in the re-attached, controlled flow, although there are also remnants of the elevated TKE in the near wall-region (Figure 2d) similar to that of the vorticity concentrations.

The centerline flow fields discussed in connection with Figure 2 only give a pseudo-2D central 'slice' of the flow, without insights into its overall 3-D structure, with or without the application of flow control. As the fluidic oscillators are spaced at discrete, equally-spaced segments along the span, it is clearly expected that there would be variation in the spanwise topology of the flow, presumably with some spatial periodicity. This aspect was also addressed in other flow control experiments, as assessed in the introduction, that suggested the physical mechanism for flow reattachment

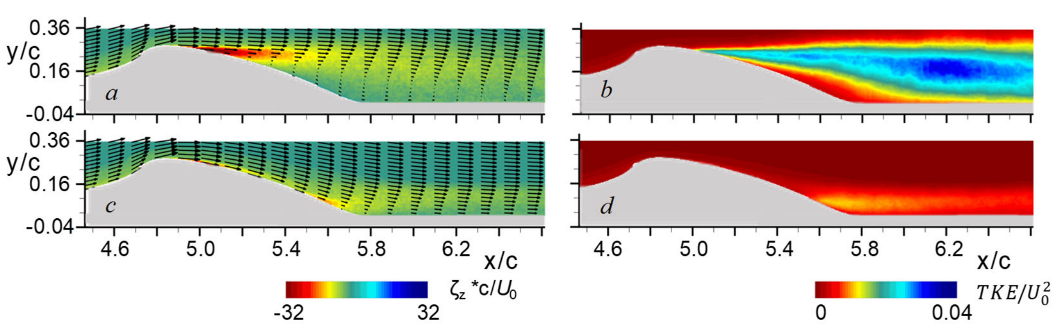

Figure 2. *Raster plots of the mean vorticity with overlaid mean velocity profiles (a, c) and the turbulent kinetic energy (b, d) at $M = 0.25$ and for the jet momentum coefficient $C_\mu \cdot 10^3 = 0$ (a, b) and 2.1 (c, d).*

stems from the production of counter-rotating vortex pairs due to the segmented flow control elements. This investigation addresses some of the structural differences the actuation brings to the flow, as well as their implied flow attachment mechanism. It should be emphasized, though, that these inferences are based on the ensuing ensemble averaged fields of the measured stereo PIV planes. Hence, they should be considered as underlying mechanisms rather than instantaneous flow events. To highlight the differences between the average flow fields and any of its instantaneous constituents, Figure 3 shows the ensemble averaged vorticity fields at $x/c = 5.54$ for the unactuated (Figure 3a) and actuated flow at $C_\mu \cdot 10^3 = 2.1$ (3c) and one sample frame of the instantaneous vorticity for each condition (Figures 3b and c, respectively). The instantaneous frames shown are reconstructed using 40 modes of the vorticity based proper orthogonal decomposition (POD). The POD reconstruction was applied to "filter out" the smallest scales and highlight the dominant vorticity structures. The instantaneous fields (Figures 3b, d) show a much richer and complex flow field than those of the average fields (Figures 3a, c), as expected, although it can be clearly seen in Figure 3d that there are also similarities in the shapes of the vorticity concentrations as well as their locations compared to what is seen in the average field (Figure 3c). The other important feature to note is that, although each instantaneous 'bundle' of vorticity consists of concentrations of different senses of vorticity, each group has a prevailing structure that presents as a single sense vortical structure in the mean. This is exactly what is considered as the underlying flow structure discussed in the paper, and the underlying attachment mechanisms that are associated with it.

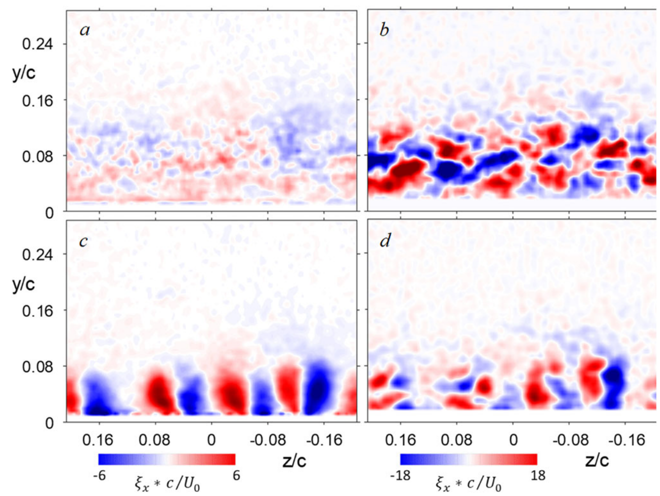

Figure 3. *Ensemble-average (a,c) and instantaneous POD-reconstructed (b,d) streamwise vorticity contour plots for the base (a,b) and the flow controlled with $C_\mu \cdot 10^3 = 2.1$ (c,d) over the spanwise field of view at x/c = 5.54. Note the ensemble average and instantaneous vorticity plots are shown with different scales to highlight the structural composition.*

The average velocity fields can give an initial insight into the structure of the flow before examining any type of vortical motion implied by the averaged vorticity fields. The spanwise distribution of the streamwise velocity (U) and its associated changes with flow control are shown as waterfall plots in Figure 4 for two stereo PIV planes located at $x/c = 5.26$ and 5.72, for varying actuation levels of $0 < C_\mu \cdot 10^3 < 2.1$. The vertical displacement from the wall (y/c) is overlaid with the scaled streamwise velocity, which is predominantly positive and as such adds in the positive y/c direction. The unactuated flow (Figure 4 a, f) is relatively uniform across the spanwise extent of the plane and also

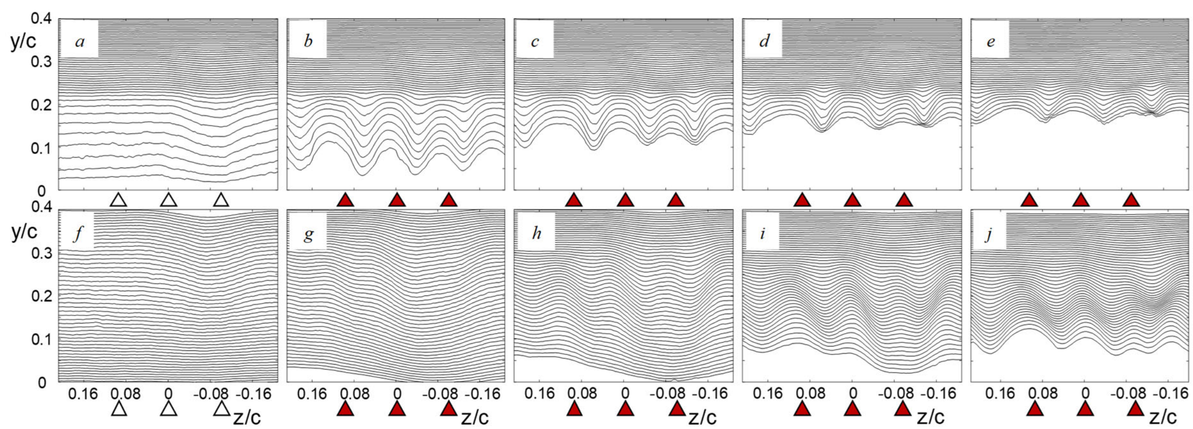

Figure 4. *Waterfall plots of the mean out of plane velocity (U) for varying cross-stream distance y/c, for the jet momentum coefficient $C_\mu \cdot 10^3$ = 0 (a,f), 0.36 (b,g), 0.96 (c,h), 1.5 (d,i), 2.1 (e,j), and for two plane locations x/c = 5.26 (a-e) and 5.72 (f-j).*

highlights the change in the streamwise flow gradients from the upstream to downstream locations. The upstream location (Figure 4a) shows a much sharper gradient from the surface (y/c = 0) outward to the free stream. This is evident in the large spacing between the velocity contours from y/c = 0 to approximately 0.2. The downstream plane (Figure 4f) shows a smoother gradient from the surface to the apparent freestream as the flow is fully separated and has a larger region of lower velocity near the surface. The large extent of the separated region is also highlighted as there is a larger spacing in the velocity contours away from the surface from y/c = 0.2 to 0.35 before they begin to collapse back together showing the flow is approaching a near constant velocity in the freestream. As actuation is initiated at $C_\mu \cdot 10^3 = 0.36$ (Figures 4b and g), the flow near the surface drastically changes, highlighted by the undulation of the streamwise velocity near the surface in Figure 4b. These undulations are aligned with the center of the jets ($z/c \approx 0.11, 0, -0.11$) and show that they impart a higher velocity near the surface as separation is delayed and the outer, higher momentum, flow is drawn closer to the surface. However, for this lower level of C_μ, the flow re-separates before reaching the downstream plane (Figure 4g). There does remain an imprint of the actuators effect on the flow, especially seen in the remnant undulations in the outer region between $0.1 < y/c < 0.3$. As C_μ is increased up to $C_\mu \cdot 10^3 = 2.1$, there is clearly an increase in the near wall velocity in the upstream plane (x/c = 5.26) as the imprint of the jets becomes more significant. This is both due to the entrainment of the outer flow, as well as the increased jet velocity. Furthermore, as the flow becomes fully attached over the whole domain at $C_\mu \cdot 10^3 = 2.1$, the remnants of the actuators effect persist into the downstream measurement domain (Figure 4j), which show similar features as in the upstream plane, although the velocity magnitude and its gradients are lower due to the diffusive test geometry that imposes adverse pressure gradient. The streamwise velocity gradients seen in Figure 4 point to domains of shearing effect of opposing senses between the jets, as the streamwise velocity is higher at the centerline of the actuators. This shearing effect initially develops opposing senses of vorticity in the positive y direction (ξ_y) along the surface of the model. This forming sense of vorticity begins to tilt and advect downstream due to the velocity deficit near the surface, which gives rise to streamwise vortices in the time-average sense, and an initial link to the attachment mechanism due to the initial interaction between the flow control jets and the oncoming flow.

Similar to the distributions of the streamwise velocity, Figure 5 shows waterfall plots of the in-plane vertical velocity component (V) for the two stereo PIV planes located at x/c = 5.26 and 5.72, for varying actuation levels of $0 < C_\mu \cdot 10^3 < 2.1$. Again, the vertical velocity is added to the spanwise distance from the wall. As the in-plane velocity is predominantly negative (towards the surface) in the measurement planes and much lower magnitude than the streamwise velocity, the vertical domain of these plots shows a tighter constriction of the spanwise contours, as well as a significant negative stretching as the outer flow is drawn towards the surface for higher levels of C_μ with increasing flow attachment throughout the measurement domain. Like with the streamwise velocity, the unactuated flow (Figure 5a, f) shows nearly spanwise uniformity across the measurement domain, with flow closer to the surface (y/c = 0) reversed (positive V, away from the surface) in the separated region. As actuation is initiated at $C_\mu \cdot 10^3 = 0.36$ (Figures 5b and g), the flow response is indicated by the undulation of the vertical velocity near the surface. Similar to the streamwise velocity (Figure 4), the outer flow is pulled closer to the surface in the presence of the jets, especially on the jet centerlines ($z/c \approx 0.11, 0, -0.11$). Again, due to the flow re-separating for this level of actuation, the downstream plane in Figure 5g only shows slight remnants of the presence of the jets as the flow begins to return to the unactuated

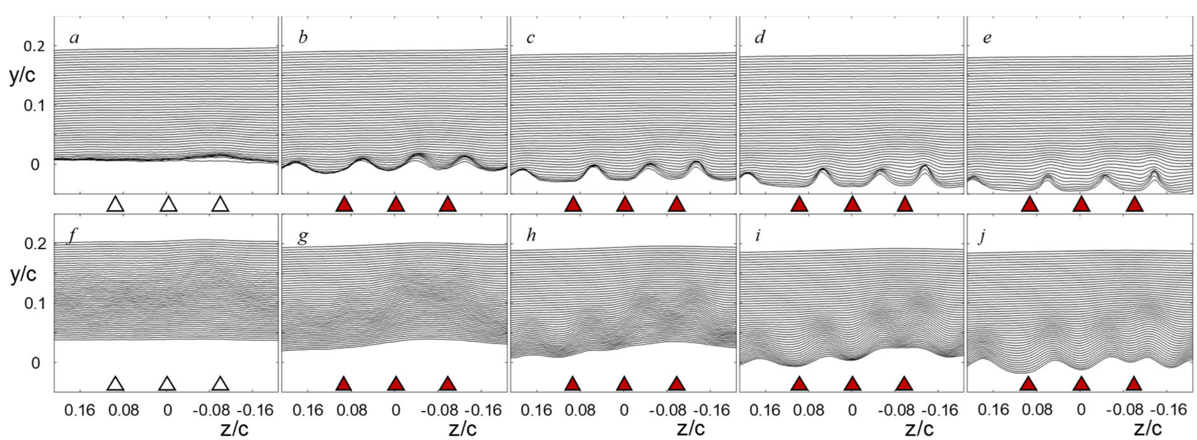

Figure 5. *Waterfall plots of the mean in-plane vertical velocity component (V) for varying cross-stream distance y/c, for the jet momentum coefficient* $C_\mu \cdot 10^3$ *= 0 (a,f), 0.36 (b,g), 0.96 (c,h), 1.5 (d,i), 2.1 (e,j), and for two plane locations x/c = 5.26 (a-e) and 5.72 (f-j).*

condition. Further increase of flow control increases the vertical velocity on the centerlines of the jets, while also increasing the gradient between the centerlines of the jets (peaks in actuated cases), clearly shown in Figures 5c-e. As these peaks (i.e. gradients) become sharper, it also indicates enhanced shearing effect caused by the jets that would result in a higher in-plane entrainment towards the jet centerline, and furthermore would result directly in the development of streamwise vorticity. As flow remains attached throughout the measurement domain for the highest actuated condition ($C_\mu \cdot 10^3 = 2.1$, Figure 5e,j) the near wall undulations remain present through the downstream plane, although the vertical velocity and gradients are reduced due to the imposed adverse pressure gradient.

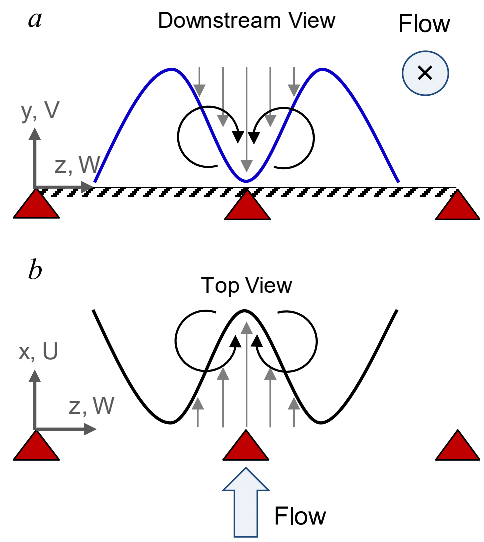

Figure 6. *Schematics of the mean vortex formation in the downstream (a) and top (b) view. Jet locations are marked by red triangles, and coordinate system is shown for reference.*

The undulations present in the (mean) velocity fields imply significant levels of shearing across the span of the measurement domain due to the presence of the actuation. This shearing effect gives rise to associated concentrations of vorticity and due to their presence, having a preferential sense of rotation. The resulting ensemble averaged vorticity concentrations based on the waterfall plots of Figure 5 are shown schematically in Figure 6 for a streamwise (Figure 6*a*) and top (Figure 6*b*) view. The coordinate system, jet locations, surface, and representative velocity contour (blue line for *V* velocity, and black line for *U* velocity) are shown for each view. The grey arrows represent the velocity magnitude and direction within the velocity contours, and the black circles with arrows show the entrainment and the shearing effect direction. Figures 4 and 5 imply that the streamwise velocity induces cross-stream vorticity (ξ_y) due to the entrainment along the centerline of the jets (and higher local velocity due to the reduction of separation and displacement of high momentum fluid near the surface), while the vertical velocity directly induces streamwise vorticity (ξ_x) as the fluid near the centerline of the jets creates a shearing in-plane effect. A streamwise view following the flow direction is shown in Figure 6a, with a representative profile (blue wavy line) of the in-plane vertical velocity with flow control (similar to that of the waterfall plots in Figure 5) showing entrainment towards the jet centerline indicated by grey arrows. This velocity distribution clearly shows the direct development of the streamwise vorticity (ξ_x, indicated by black circles with arrows indicating rotation sense) due to the shearing effect caused by the flow control increasing the vertical velocity on the centerline of the jets. Similarly, Figure 6b shows a schematic of the streamwise velocity (black wavy line) from a top view, which also shows the development of the cross-stream vorticity (ξ_y, black circles with arrows indicating rotation sense) due to the higher velocity along the jet centerline. The cross-stream vorticity present in Figure 6b would tilt downstream due to the velocity deficit near the surface, and couple to the same streamwise vorticity sense as developed in Figure 6a. These entrainment mechanisms suggest similarity of this flow control application to the vorticity generation of a wall-jet in the absence of cross-flow [26], unlike the typical jet in crossflow. This type of wall-jet interaction creates a hairpin-like structure along the jet issuance direction, which then tilts and advects downstream. These coupling effects should therefore generate coherent streamwise vorticity concentrations and could create counter-rotating vortex pairs associated with jets in crossflow. It is also important to note that despite being discussed in terms of the time average, this shearing effect, vorticity concentration generation, and ensuing attachment mechanism still applies in the instantaneous flow fields despite their more complex structure.

The ensemble-averaged PIV flow fields indicate the presence of multiple pairs of vorticity concentrations of opposing sense. To examine the formation and development of these streamwise vorticity concentrations due to the flow control, the flow control parameter C_μ is incremented within a narrow range for a single plane and the resulting velocity and vorticity distributions are shown in Figure 7 for the plane located at $x/c = 5.54$, and $0.36 < C_\mu \cdot 10^3 < 1.2$. The actuation cases selected are such that the lowest actuation levels are not sufficient to attach the flow beyond the measurement domain, while Figures 7d,i show cases where the flow is attached beyond the shown spanwise plane. Contour plots of the streamwise velocity component (U) are shown in Figure 7a-e, as the upstream view. As flow control is incremented slightly for the cases shown from Figure 7a to Figure 7e, the effect of the actuators is clearly demonstrated. The flow control brings the outer, higher momentum flow closer to the surface, as indicated by the reduction in the low (and reversed flow) near-wall momentum region in the contours from about $y/c = 0.05$ to 0.03. As the outer flow is brought closer, it also shows a clear segmentation of the low momentum region, with the higher

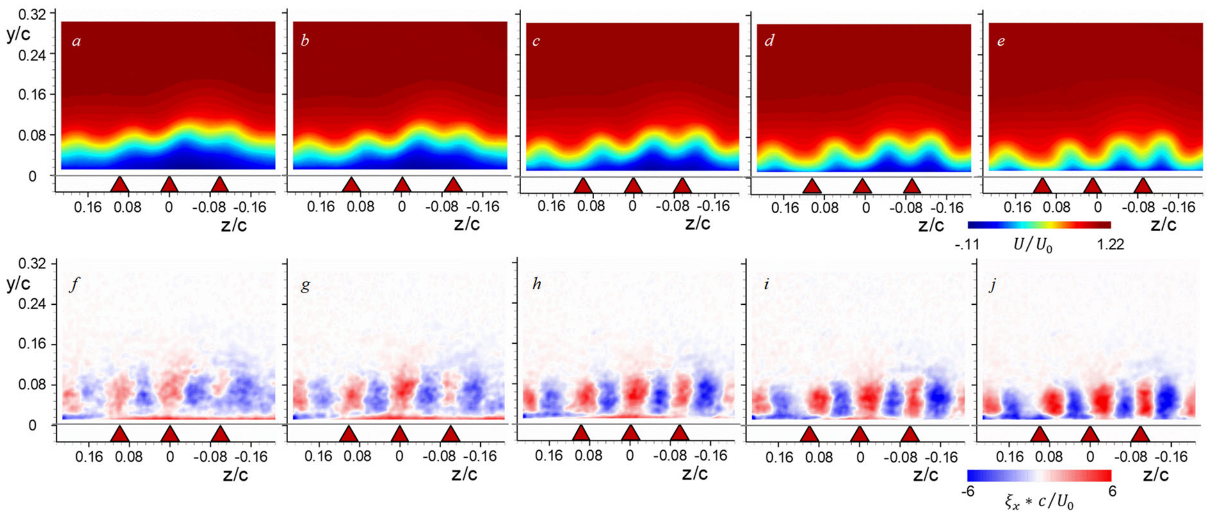

Figure 7. *Color raster plots of mean streamwise velocity component (U) (a-e) and vorticity (f-j) for varying spanwise distance y/c, for the jet momentum coefficient $C_\mu \cdot 10^3$ = 0.36 (a,f), 0.46 (b,g), 0.70 (c,h), 0.96 (d,i), 1.2 (e,j), and the plane location x/c = 5.54.*

velocity being located, again, on the centerlines of the jets ($z/c \approx 0.11, 0, -0.11$). These peaked regions, as discussed in the waterfall plots of Figure 4, are where shearing effects are taking place as the higher momentum flow begins to drag the lower momentum flow between the jets. The higher actuation levels ($C_\mu \cdot 10^3 = 1.2$), show a drastic peak and valley pattern, even though the overall momentum coefficient is only slightly changed between these sweeping conditions through attachment. These deeper peaks and valleys are an indication of stronger shearing effects.

For the same incremented actuation levels and upstream views, the streamwise vorticity concentrations are shown in Figure 7f-j. The first feature to note is the development of vorticity of opposing sense at the jet centerlines ($z/c \approx 0.11, 0, -0.11$), with counter-clockwise (positive) streamwise vorticity on the right side of the actuator centers, and consequently clockwise (negative) sense on the left. In the time average sense, these vorticity concentrations suggest entrainment towards the centerline of the jets. This spanwise pattern of opposing vorticity concentrations occurs across the extent of the measurement domain and would persist throughout the extent of the actuator array, and the sense of vorticity is clearly developed due to the organization of the flow by the control jets interaction with the flow. One important note is the correlation between the streamwise velocity Figure 7a-e and the development of the streamwise vorticity Figure 7 f-j. As the flow control is incremented ($0.36 < C_\mu \cdot 10^3 < 1.2$) from the flow in Figure 7f to that of Figure 7j, the streamwise vorticity becomes both intensified and drawn towards the surface. As the actuation is increased, the lower extent of the vorticity concentrations move closer to the surface ($y/c = 0$) and also intensify while becoming more coherent. Clearly, the vorticity concentrations follow the trends observed in the streamwise velocity contours. As the peaks and valleys between the jets deepen, consequently the vorticity in these regions also intensifies.

As discussion of Figure 7 indicates, there is a clear development of a spanwise pattern of vorticity concentrations of opposing sense (i.e. counter-rotating vortex pairs) due to the application of flow control considered at a given streamwise location. Further analysis considers the flow structure evolution in both the streamwise and spanwise extent. Figure 8 shows the topology and formation of streamwise vortices for three stereo PIV planes located at $x/c = 5.26$, 5.54, and 5.72, and for varying actuation levels of $0 < C_\mu \cdot 10^3 < 2.1$. For a given streamwise plane and increasing actuation level (left to right columns) in Figure 7, the flow progresses from fully separated in the unactuated condition on the left (Figure 8 a,f,k) to fully attached over the entire streamwise measurement domain at $C_\mu \cdot 10^3 = 2.1$ (Figure 8 e,j,o). For each plane considered, the nominally attached conditions up to the measured stereo PIV plane are seen in Figures 8 b, h, n, and increasing actuation further (left to right) beyond these flow fields delays separation farther in the streamwise direction. Clearly, the unactuated flow (Figure 8 a, f, k) shows no coherent structure as the flow is fully separated. As flow control is applied at low C_μ ($C_\mu \cdot 10^3 = 0.36$, Figure 6 b, g, l), pairs of counter rotating vortex pairs are formed across the span of the upstream measurement domain. All vortices show positive (counter-clockwise) sense of vorticity on the right side of the jets, and opposing negative (clockwise) on the other, as the flow issues out of the page. For this low level of C_μ, the vortices do not extend far in the downstream direction as the next plane (progression Figure 8 b, g, l) already shows the intensity of the vorticity to be decreasing and becoming less coherent across the measurement plane. By the farthest station (Figure 8l) the vorticity begins to resemble that of the

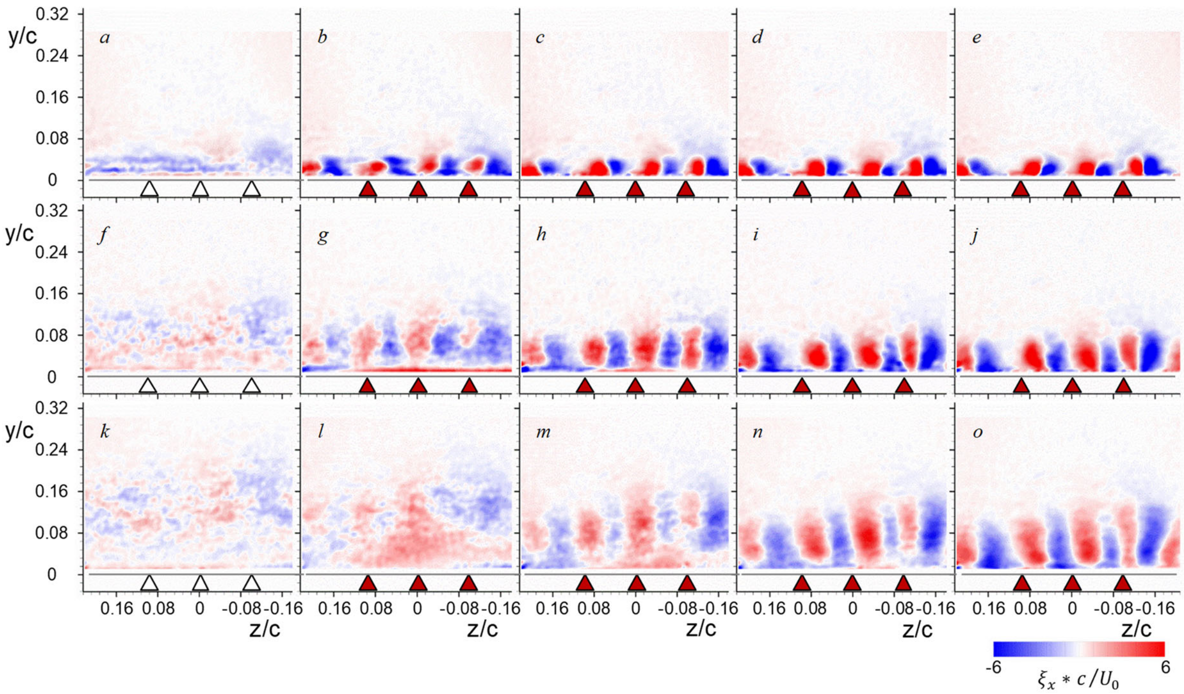

Figure 8. *Evolution of the mean streamwise vorticity for the base flow $C_m{\cdot}10^3$ = 0 (a,f,k) and actuated flows for $C_\mu{\cdot}10^3$ = 0.36 (b,g,l), 0.96 (c,h,m), 1.5 (d,i,n), 2.1 (e,j,o). For three streamwise planes x/c = 5.26 (a-e), 5.54 (f-j), and 5.72 (k-o).*

base flow and the span-wise mixing has completely taken over as the flow re-separates. When C_μ is increased for a given plane (x/c = 5.54, Figure 8 f-j) the formation of the vortices can be clearly seen. As actuation is initially applied (Figure 8g), the imprint of the counter rotating vortices can be seen in the outer flow away from the wall. As the C_μ is increased further, these vortices intensify and begin to move towards the wall. In all locations, increasing the jet strength intensifies the vorticity and draws the outer flow closer to the surface. It can clearly be seen for the highest actuation level that as the flow is attached and progresses downstream (Figure 8 e, j, o), the vortices become stretched into the outer flow due to the presence of the adverse pressure gradient. Furthermore, these vortices remain organized in counter-rotating pairs while stretching away from the near wall region, even as the flow becomes attached along the model surface, with the vorticity concentrations shown indicating on average an upwelling of the flow in between the jets and consequently a downwelling at the jet centerlines.

IV. Actuation-Effected Turbulent Flow Characteristics

The mean vorticity concentrations discussed in Section III point to a structural flow development in the average sense due to the presence of the actuation. Further insight into the actuation effect on the flow development is sought by unsteady flow characterization. Similar to the vorticity distribution shown in Figure 8, Figure 9 shows the development of the turbulent kinetic energy (TKE) for varying actuation levels along with the downstream flow evolution. The unactuated flow (Figure 9 a, f, k) shows that the elevated TKE is contained within the separating shear layer and remains relatively uniform across the span of the measurement domain. As actuation is applied ($C_\mu{\cdot}10^3$ = 0.36, Figure 9 b, g, l), it is seen that in the upstream plane (Figure 9b) the actuators begin to break up the layer of high TKE seen in the unactuated flow into discrete segments. Consequently, the high concentration of TKE remains "trapped" in between the jets. As the flow evolves downstream, however (Figure 9g), the flow re-separates and the shear layer begins to re-form, and these discrete segments begin to reconnect. Despite the flow re-separation, there is still an imprint of the jet effect seen at the outer layer of the TKE that persists down to the last measurement plane (Figure 9l). As the actuation coefficient is increased up to $C_\mu{\cdot}10^3$ = 2.1 at the upstream measurement plane (Figure 9e), the TKE within the shear layer is significantly decreased with overall peak levels reduced compared to the unactuated flow, and the only peak locations remain located between the jet centers. This trend continues for each measurement domain in Figure 9, and shows that as actuation is applied, the overall peak TKE levels become

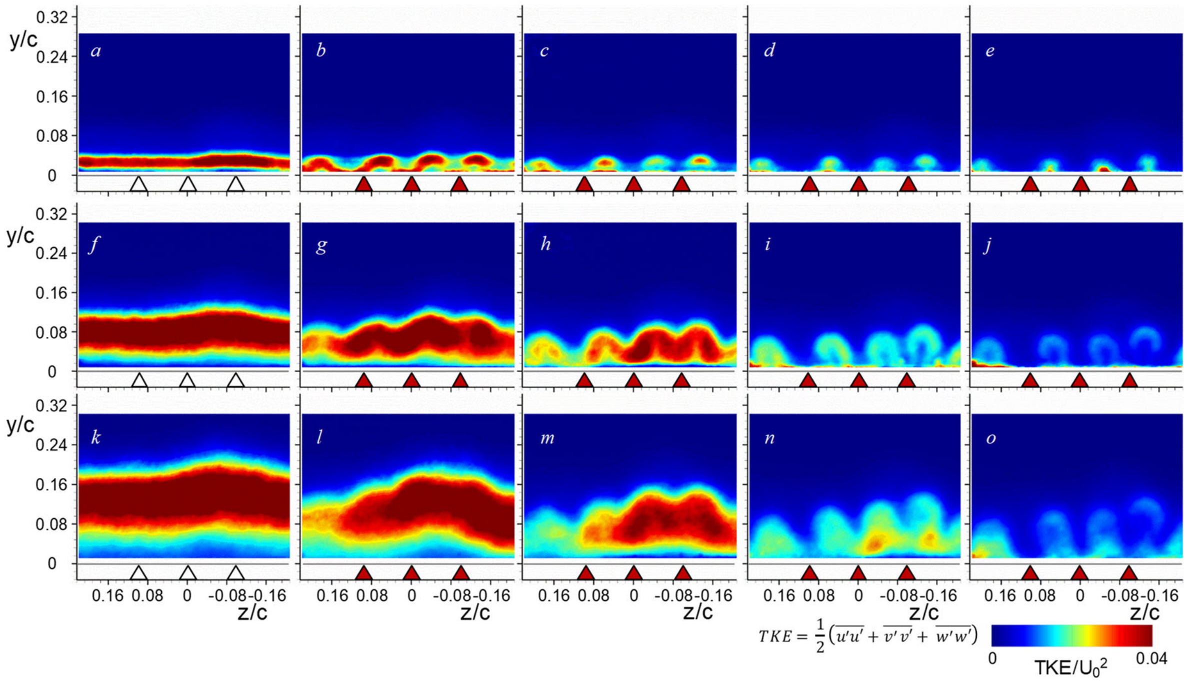

Figure 9. *Evolution of the turbulent kinetic energy for the base flow $C_m \cdot 10^3 = 0$ (a,f,k) and actuated flows for $C_\mu \cdot 10^3 = 0.36$ (b,g,l), 0.96 (c,h,m), 1.5 (d,i,n), 2.1 (e,j,o). For three streamwise planes x/c = 5.26 (a-e), 5.54 (f-j), and 5.72 (k-o).*

significantly reduced compared to that of the base/unactuated flow. Another notable effect is the development and outline of the structure between the jets. The vorticity concentrations shown in Figure 8 indicate on average an upwelling of the flow in between the jets. The TKE begins to highlight some further characteristics of these vortical structures between the jets. These structures show up as lobes, or halos, of concentrated TKE as clearly seen in Figure 9 i, j, o, for higher levels of actuation and downstream flow progression. In addition, these structures become stretched away from the surface due to the presence of the adverse pressure gradient. Furthermore, these structures also persist far outside of the near wall region.

A closer view at the TKE evolution across the jet interaction domain is shown in Figure 10, where profiles of the TKE are extracted in the spanwise direction from the jet centerline $z/c = 0$ to approximately the half width in between the jets (at $z/c = 0.048$). Such profiles are plotted for the three PIV planes located at $x/c = 5.26$, 5.54, and 5.72, and for varying actuation levels from $0 < C_\mu \cdot 10^3 < 2.1$. The individual profiles are color-coded with progressively darker color from the centerline (light red lines) to the half width between the jets (black lines). When considering the unactuated flow (Figure 10 a, f, k), it is apparent the spanwise distribution of the TKE is uniform (void of coherent spanwise structures) as the profiles collapse onto each other. Furthermore, it shows the TKE peak is located in the separated shear layer and as the flow progresses downstream, the peak displaces farther from the wall and the overall region of TKE thickens about the maximum level. These base flow characteristics of the TKE distribution are altered in the controlled flow. For example, if the flow control parameter is varied from $0 < C_\mu \cdot 10^3 < 2.1$, it is clear that the overall TKE is significantly reduced, while also shifting the peak towards the surface with increasing actuation in any of the examined planes ($x/c = 5.26$, 5.54, or 5.72). When examining the plane $x/c = 5.54$ (Figure 10 f-j), the peak base flow TKE levels are reduced approximately 77% due to the flow control. The peak location also shifts towards the surface from $y/c \approx 0.08$ to 0.06. Another perspective is gained from examining the flow evolution in the downstream direction for a given flow control parameter. For instance, at $C_\mu \cdot 10^3 = 1.5$ (Figure 10d, i, n), there is not a significant change in the peak levels of the TKE in the downstream direction, and furthermore, the peak locations (and overall cross-stream extent) actually grow and diffuse away from the surface due to the imposed adverse pressure gradient along the model. This evolution is in agreement with the flow structures growing and diffusing in the streamwise direction, while remaining organized.

An insight into the spanwise flow structure can be gained by examining the distributions of spanwise profiles of the TKE in Figure 10. While there is a full spanwise uniformity of the base flow (Figure 10 a, f, k), the TKE loses its spanwise uniformity even with the lowest actuation level at $C_\mu \cdot 10^3 = 0.36$ (Figure 10 b, g, l). The upstream plane

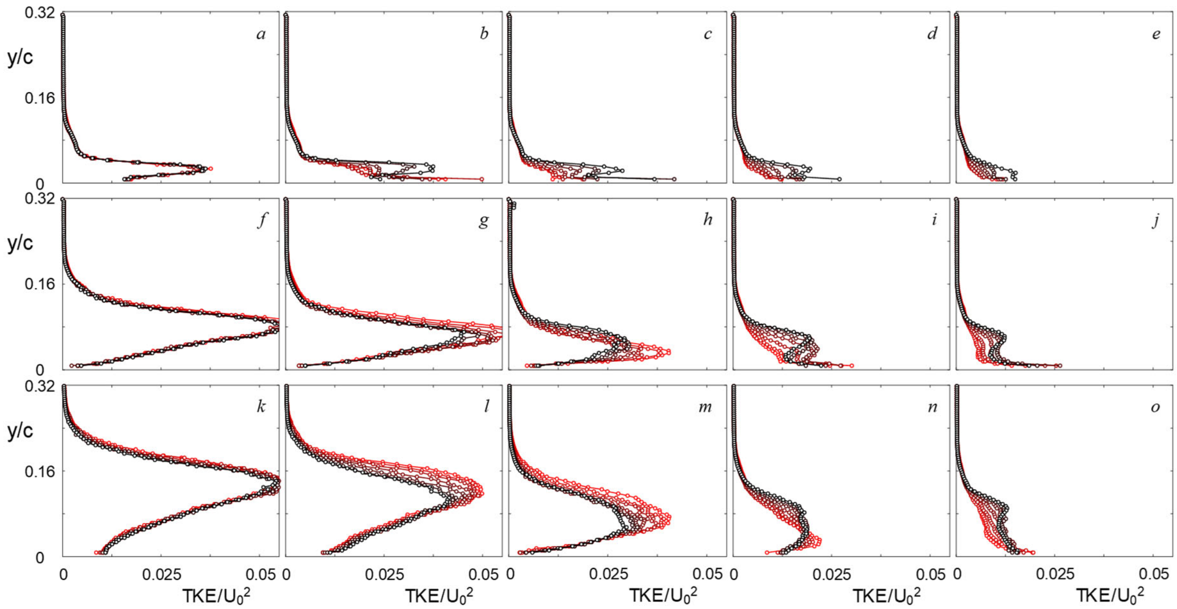

Figure 10. *Equidistant profiles of the TKE from z/c = 0 (red line) to 0.048 (black line), for the base flow* $C_\mu \cdot 10 = 0$ *(a,f,k) and actuated flows for* $C_\mu \cdot 10^3 = 0.36$ *(b,g,l), 0.96 (c,h,m), 1.5 (d,i,n), 2.1 (e,j,o), and at the three streamwise locations x/c = 5.26 (a-e), 5.54 (f-j), and 5.72 (k-o). Darkening color indicates spanwise progression from z/c = 0 to 0.048.*

shows the segmentation of the shear layer as the peak levels coincide with the half distance between the jets, and there is even a magnitude reduction on the centerline of the jets as compared to the unactuated flow. As the flow progresses downstream, however (Figure 10 g and l), the profiles begin to resemble those of the unactuated conditions, as they begin to collapse again, although not returning to complete spanwise uniformity and thus preserving some remnants of the jet imprint. As the flow control is increased and the 'halo' structures/features discussed in Figure 9 become more distinct in the downstream planes for $C_\mu \cdot 10^3 = 1.5$ (Figure 10 d, i, n), there is a notable difference between the spanwise distribution of the TKE. First, the halo/lobed pattern can be clearly seen in Figure 10i, as the profiles develop a double inflection as they traverse away from the jet centerline. As the profiles migrate to the center of one of the structures, the peak TKE levels continually shift away from the surface, until they reach a peak at the center of the top of the structure and then decay towards the free stream.

Besides the total TKE discussed in Figures 9 and 10, it is insightful to examine how the TKE energy producing and dissipating terms evolve in the controlled flows. The turbulent production and dissipation in the flow are shown in Figure 11 for the stereo PIV plane located at $x/c = 5.26$, and for varying actuation levels of $0 < C_\mu \cdot 10^3 < 2.1$. The production terms are calculated as $\Pi = -\langle u_i u_j \rangle \overline{S_{ij}}$ and the dissipation rate as $\varepsilon = 2\nu\langle s_{ij} s_{ij}\rangle$. Both of these estimates exclude the derivatives in the x-direction ($\partial/\partial x$), except for where they can be inferred from continuity (i.e., $\partial u/\partial x$). It can be argued that the local streamwise variations about the measured spanwise PIV planes is small compared to the in-plane variations, which is inferred from the prior planar measurements [28]. Furthermore, Namgyal and Hall [25] made similar assertions in the case of a turbulent wall jet.

Similar to the TKE contours, the base flow (Figure 11a, f) turbulent production and dissipation rates appear nearly spanwise uniform across the measurement domain and located within the shear layer near the surface. Still, it seems that the peak bands of the production and dissipation rate do not exactly line up spatially and that the peak dissipation rate is better aligned with the upper band of the production distribution. Activation of the flow control at the lowest C_μ (Figure 11b and g) shows that as the jets begin to segment the shear layer, TKE production levels are reduced about the jet issuance. Interestingly, although the dissipation rate also follows the segmentation of the layer, the dissipation rate becomes increased near the surface along the jet locations. With continuous increase in C_μ (left to right in Figure 11), the overall peak production levels become progressively reduced compared to the base levels. In addition, there is a significant local suppression in the production term about the jets' locations. The dissipation rate, however, exhibits a different trend. Although it forms similar halo structures in between the jets, they are not disconnected, as the increased levels of the dissipation rate along the surface interconnect the halo structures, contrary to segmentation observed in the spatial distribution of the TKE production. Another difference is that it appears that the dissipation

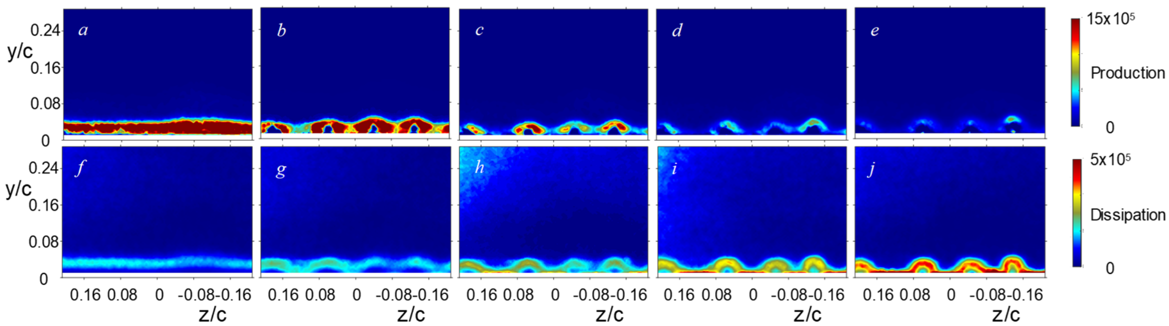

Figure 11. *Turbulent production P (a-e) and dissipation rate e (f-j) at x/c = 5.26 for the base (a,f) and actuated flows for* $C_\mu \cdot 10^3$ *= 0.36 (b,g), 0.96 (c,h), 1.5 (d,i), 2.1 (e,j).*

rate increases in magnitude with increases in C_μ, contrary to the production rate. Lastly, there is again a mismatch between the spatial distributions of the peak production and the peak dissipation within the halo structures. In the controlled flow, the peak dissipation rates are aligned with the lower band of the peak TKE production halo structures (e.g., compare Figures 11e and j). This analysis suggests that the reduced levels of TKE about the jet locations result from both reduced production and increased TKE dissipation rate in the controlled flow. Furthermore, the misalignment of the peak production and dissipation within the halo structures, with the dissipation rate being offset towards the surface, is in agreement with the resulting halo structure of the elevated TKE in the controlled flow previously discussed in connection with Figure 9.

The turbulent production and dissipation characteristics in the flow are somewhat different for the farther downstream plane located at x/c = 5.72, as shown in Figure 12. The turbulent production and dissipation rates are again tied to the shear layer, which is displaced further away from the surface as the flow separation grows downstream. Consequently, the extent of the elevated levels of production and dissipation is expanded as well, compared to Figure 11. Although being spanwise nominally uniform, these distributions show some growing undulation, which was visible upstream Figure 11) as well. As the actuation coefficient increases from left to right in Figure 12, and separation is delayed, the effects of the jets bear some similarities and differences to those observed upstream (Figure 11). For lower actuation levels (Figure 12b and c), the shear layer begins to segment and divide similar to the upstream plane, although the production domain is broken up away from the wall. As C_μ begins to increase further, the production levels continue to segment, reduce in peak intensity, draw closer to the wall, and in the highest levels again form the discrete 'halo' signatures. Similar to the upstream plane in Figure 11, the outer flow structures that contain the production are significantly reduced compared to that of the unactuated flow. In one addition relative to the upstream plane, the production term develops the highest magnitudes at the stems of the formed halos, which was not observed in the upstream plane. The dissipation rate (Figure 12 f-j), like the production term, also initially remains closely tied to the separated shear layer and has undulated intensity for the base flow (Figure 12f). The lowest level of C_μ (Figure 12g) initially amplifies the undulations, without appreciable difference in the peak levels. Further increase from left to right, shows the growing segmentation, although never as pronounced as in the corresponding production term. Even at the highest actuation level, the local area of dissipation appears quite diffused across the domain where the halo-like structures appear in the production. Contrary to the increased levels of the

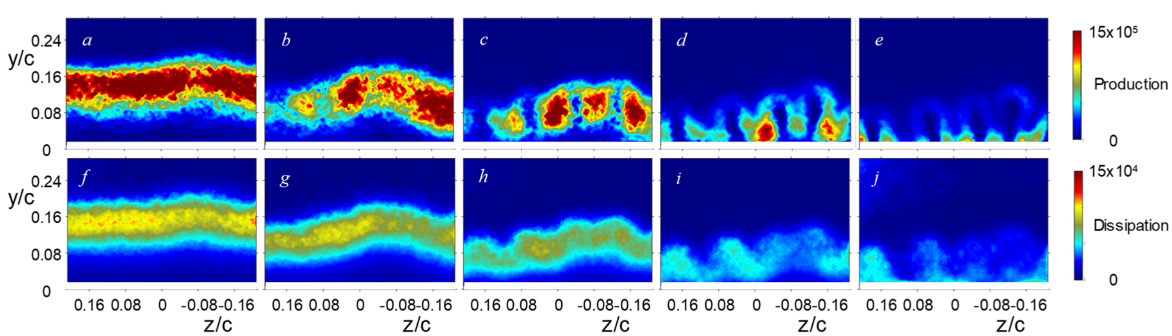

Figure 12. *Turbulent production Π (a-e) and dissipation ε (f-j) at x/c = 5.72 for the base flow (a,f) and actuated flows for* $C_\mu \cdot 10^3$ *= 0.36 (b,g), 0.96 (c,h), 1.5 (d,i), 2.1 (e,j).*

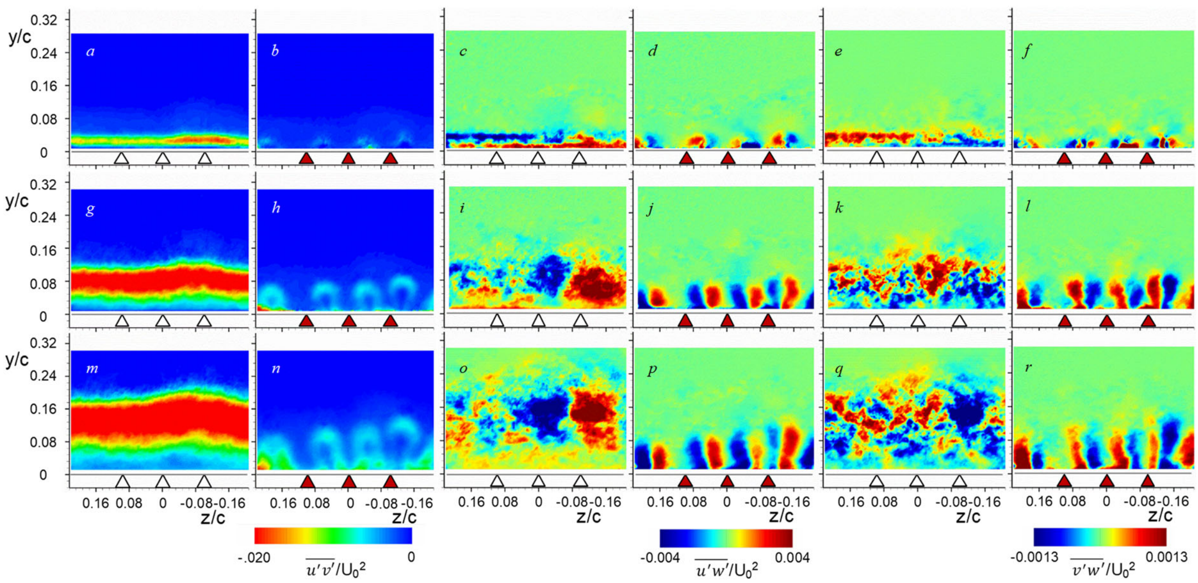

Figure 13. *Normalized Reynolds stresses for the base flow (a, c, e, g, i, k, m, o, q) and actuated flows for $C_\mu \cdot 10^3 = 2.1$ (b, d, f, h, j, l, n, p, r) and for three streamwise locations x/c = 5.26 (a-f), 5.54 (g-l), and 5.72 (m-r).*

dissipation rate with C_μ at the upstream plane (Figure 11), its magnitude in Figure 12 follows the same declining trend as in the turbulent production.

Aside from the normal turbulent stresses incorporated into the TKE energy term, additional information about turbulent stresses in the flow is assessed from the three normalized Reynolds stresses ($\overline{u'v'}$, $\overline{u'w'}$, and $\overline{v'w'}$) shown in Figure 13, for the unactuated base flow and for the highest actuation ($C_\mu \cdot 10^3 = 2.1$). They are also shown for the three streamwise measurement planes to address the development of the stresses under the application of flow control. Out of all the cases depicting the base flows (Figure 13 a, c, e, g, i, k, m, o, q), only the $\overline{u'v'}$ shows a structure similar to the TKE distribution, where the high levels are concentrated within the separating shear layer. The other two Reynolds stresses ($\overline{u'w'}$, and $\overline{v'w'}$), nominally do not show significant spanwise coherence or relation to the separating shear layer, and somewhat mimic what is seen in the vorticity for the same conditions in Figure 8. However, a large-scale paired structure seen in Figure 13i and o might be related to the spanwise undulations of the shear layer noted earlier. It is also noted that the normalized shear stress ($\overline{u'v'}$) levels are at least an order of magnitude higher than that of the other two Reynolds stresses ($\overline{u'w'}$, and $\overline{v'w'}$). When the flow control is used to fully attach the flow at $C_\mu \cdot 10^3 = 2.1$ (Figure 13b, h, n), there is an overall decrease in the magnitude of the shear stress ($\overline{u'v'}$), compared to the base flow, as well as a coherent restructuring into the familiar 'halo' shapes seen in the TKE contours previously. The flow control, again, segments the ($\overline{u'v'}$) stress in the spanwise direction, and even as the flow is reattached, these structures continue to ride outside of the near wall region and also stretch away from the wall as the flow progresses downstream (Figure 13b to h to n). As the shear stress ($\overline{u'v'}$) indicates a clear organization of the flow with actuation, so to do the other stresses ($\overline{u'w'}$, and $\overline{v'w'}$) demonstrate the organization of the flow. Examining the $\overline{u'w'}$ (Figure 13 d, j, p) and $\overline{v'w'}$ (Figure 13f, l, r) for the actuated conditions, the stresses show similar structure to that seen in the time averaged vorticity concentrations. The pairs of concentrations of opposing signs appear anchored in between the active jets, which clearly ties

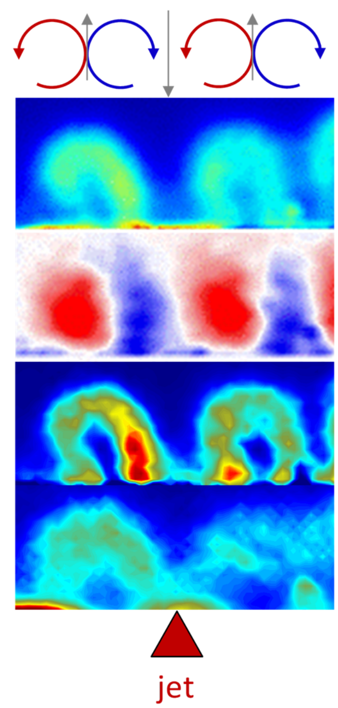

Figure 14. *Schematic, illustrating, from top to bottom, vortical field about a single flow control jet and the accompanying fields of TKE, streamwise vorticity, TKE production and dissipation rate. The sample flow fields are at x/c = 5.54 and for $C_\mu \cdot 10^3 = 2.1$ (cf. Figures 8 and 9).*

them with the jets' interaction with the flow. They also exhibit a similar stretching effect as the flow migrates downstream. Not only do the structure of the shear stress concentrations resemble those of vorticity, they also point to the sense of the local flow rotation. For example, Figure 13l shows a pocket of negative sign of stress ($\overline{v'w'}$) on the left of the center jet, and an accompanying positive pocket on the right. The negative stress sign on the jet left side implies that if there is an upward/positive fluctuation of the cross-stream component v', it would be accompanied with the negative w' fluctuation, which would be to the right in this view. Such a coupled fluctuation would correspond to a motion aligned with a rotation with a negative sense. The same analysis would predict a positive sense of rotation on the right side of the jet, based on the positive sense of stress $\overline{v'w'}$. Clearly, both of these predictions are in agreement with the senses of vorticities about the central jet already presented in Figure 8.

As discussed above, there is a clear relationship between the structure of the controlled flow fields and the ensuing turbulent characteristics. To highlight and summarize this, Figure 14 shows a schematic depicting the time averaged vortical motions about a single control jet, marked by a triangle. Lined with the schematic, the corresponding fields of TKE, vorticity, turbulent production, and turbulent dissipation rate for a sample case of $C_\mu \cdot 10^3 = 1.5$ at the streamwise plane $x/c = 5.54$ are shown. In the time-average sense, each jet induces a vortex pair such that a 'downwash' is created about the jet centerline. One of each vorticity concentration from the neighboring jets (outside of the view) are also present in the shown view, pairing with each of the central jet vortices. The color of each vortex schematic corresponds to its sense of rotation. In addition, straight arrows point in the direction of downwash along the jet centerlines and upwash in between the jets, as induced by the flow vortices. It is seen that both high levels of both the production and dissipation rate of TKE are formed in an arch about the upwelling flow, where the near-wall flow is brought upward due to the joint vortex actions. Consequently, the region of high TKE is also formed in arch structures about each of the upwelling domains. As this analysis was based on the time-averaged structure, it should be noted that these quantities are the cumulative effect of the instantaneous vorticity present (*cf.* Figure 3).

The application of flow control to the separated base flow clearly alters its spanwise structure which is tied to the scale of the spanwise spacing of the control jets, and as shown above, leads to attachment which exhibits the same spanwise periodicity. It is remarkable, that despite the spanwise variations that are effected by near-wall actuation, the outer flow can be independently scaled. Figure 15a shows several cross stream distributions of the streamwise velocity that are measured at equally-spaced spanwise positions in the spacing between the center of an actuation jet and the center of the gap between its adjacent jet ($x/c = 5.72$, $C_\mu \cdot 10^3 = 1.5$). These data show that at this streamwise location the near wall effects of the adjacent jets are nearly uniform. However, there is still clear spanwise variation in the velocity distributions in the outer flow exhibiting a secondary inflection point and larger velocity deficit towards the mid-span between the jets as a result of the upwelling or 'upwash' region in between the jets. Schatzman and Thomas [16] proposed a scaling of an outer flow over a surface in an adverse pressure gradient by the local shear layer vorticity thickness $\delta_\zeta = (U'_e - U')_{IP}/(dU'/dy)_{IP}$, and the velocity deficit $U'_d = (U'_e - U')_{IP}$, (*IP* designates the inflection point). As a result, the dimensionless length and velocity parameters are $\eta = (y' - y'_{IP})/\delta_\zeta$ and $U^* = (U'_e - U')/U'_d$ (U'_d is the velocity deficit between the 'free stream' velocity U'_e and at the inflection point U'). This scaling was also successfully applied by Peterson et al. [28] at local separation and reattachment to natural

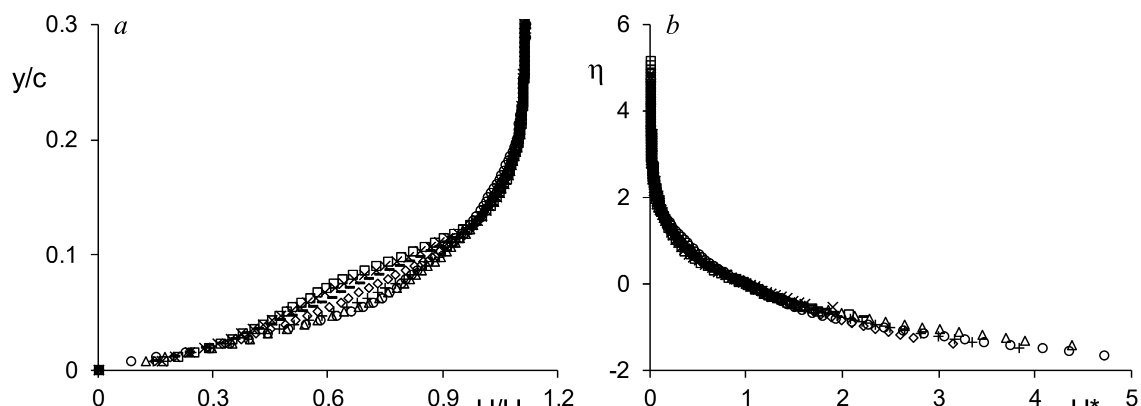

Figure 15. *Equidistant spanwise, time averaged, streamwise velocity profiles (a) from the jet centerline at z/c = 0 (○), to half way between the jets from z/c = 0.008 (△), 0.016 (+), 0.024 (◇), 0.032 (-), 0.040 (×), to 0.048 (□), and the scaled [16,17] time averaged velocity profiles (b), for the flow controlled at* $C_\mu \cdot 10^3 = 1.5$ *at the streamwise location x/c = 5.72.*

and forced boundary layers. This scaling was applied to the velocity profiles in Figure 15a, and the scaled velocity profiles are shown in Figure 15b. The collapse of the data implies that despite the spanwise differences between the local cross-stream scales of the time-averaged velocity distributions in the presence of actuation, scaling by the local vorticity layer thickness and velocity deficit yields excellent collapse of the spanwise profiles. This indicates that despite the near wall effects of the actuation, the local flow is still affected by the outer shear away from the wall and indicates that the near-wall control effectiveness is coupled to the outer flow.

V. Conclusion

Controlled modification of a separated flow domain over a 2-D curved surface modeling the suction surface of a VR-12 airfoil is investigated in wind tunnel experiments at $M = 0.25$. Actuation is applied using a spanwise array of equally-spaced fluidic oscillating jets that emanate nearly tangentially to the surface just upstream of the separated flow and operate at frequencies that are well above the unstable frequencies of the base flow. The interaction of the actuation jets with the separating flow is investigated in spanwise cross-stream planes using high-resolution stereo PIV centered about the mid-span. In the present investigations, the measurements were acquired at three streamwise positions focusing on the near-, mid-, and far-field evolutions of the base flow and its interactions with the control jets.

The present investigations show that the unactuated, separated flow above the surface is characterized by the formation of multiple strands of interacting counter-rotating streamwise vortices that appear to have little streamwise coherence. The presence of the actuation jets induces nearly spanwise-periodic alternating down- and upwash flows within the cross flow over the surface that are symmetrically centered about the jets' centers and half way between them, respectively. The interactions between the azimuthal shear layers that form about the jets and the upwash flow between them appears to organize the counter-rotating streamwise vortices in spanwise-periodic concentrations between the jets. Moreover, it is striking that the effect of the actuation is such that the time-averaged structure of vorticity concentrations between the jets is a pair of streamwise-coherent, counter-rotating vortices. Therefore, the actuation jets engender the formation of a spanwise array of counter-rotating streamwise vortex pairs downstream from the control jets in concert with the spanwise-alternating downwash and upwash flows.

Analysis of the time-averaged flow about the actuation jets indicates that the formation of the dominant streamwise vorticity concentrations is tied to 3-D shear effects similar to that of a wall jet in the absence of a cross flow and are associated with undulations of the streamwise velocity that induce cross-stream vorticity (ξ_y) and of the cross-stream velocity that induce streamwise vorticity (ξ_x). The cross-stream vorticity is tilted in the streamwise direction by the streamwise velocity deficit near the surface, and couples to streamwise vorticity of the same sense that is associated with the cross-flow shear. These streamwise vorticity concentrations persist in the streamwise direction, and the flow between the jets may lead to local separation farther downstream owing to the upwash. The upwelling regions between the active jets are associated with enhanced production and dissipation rates of turbulent kinetic energy (TKE) and the turning of the upwash flow leads to the formation of distinct halo structure about the upwash region. These data indicate that the jets reorganize the production and dissipation of TKE due to the upwelling of low-momentum fluid from the surface that mixes rapidly with the outer high momentum fluid. Consequently, the downwash region located about the jet centers leads to transport of high momentum fluid towards the surface that suppresses the TKE production and intensifies the dissipation in the near field planes while suppressing it in the far field. Overall, the TKE levels in the spanwise domains that become attached by the flow of the actuation jets are lower compared to the separated base flow.

Finally, although the actuation effects spanwise periodicity in the time-averaged attached flow, which is also clearly present in the outer flow, it is remarkable that the outer flow can be spanwise-scaled. When the spanwise variations of the streamwise velocity subside (following merging of the actuation jets) near the surface, the spanwise variations in the outer shear layer are evident from cross stream distributions of the streamwise velocity that exhibit secondary inflection points and larger velocity deficits between the jets. Despite the spanwise differences between the local cross-stream scales of the time-averaged velocity distributions in the presence of actuation, scaling by the local vorticity layer thickness and velocity deficit yields excellent collapse of the spanwise profiles. This implies that despite the near wall effects of the actuation, the local flow is still affected by the outer shear away from the wall and indicates that the near-wall control effectiveness is coupled to the outer flow.

Acknowledgments

Funding provided by the Georgia Tech Vertical Lift Research Center of Excellence

References

[1] Ethier, C. R., Prakash, S, Steinman, D.A., Leask, R.L., Couch, G.G. and Ojha, M., “Steady flow separation patterns in a 45 degree junction,” *J. Fluid Mechanics*, **411**, pp. 1-38, 2000.

[2] Blanckaert, K., “Flow separation at convex banks in open channels,” *J. Fluid Mechanics*, **778**, pp. 432-467, 2015.

[3] Papadopoulos, G., and. Otugen, M. V., “Separating and reattaching flow structure in a suddenly expanding rectangular duct,” *J. Fluids Eng*., 117, pp. 17-23,1995.

[4] Yang, William, and Benny Kuan. "Experimental investigation of dilute turbulent particulate flow inside a curved 90 bend." *Chemical Engineering Science*, 2006; Vol 61 no. 11, pp. 3593-3601.

[5] Suzuki, T., Colonius, T. and Pirozzoli, S., “Vortex shedding in a two-dimensional diffuser: theory and simulation of separation control by periodic mass injection,” *J. Fluid Mechanics*, **520**, pp. 187-213, 2004.

[6] Amitay, Michael, Dale Pitt, and Ari Glezer. "Separation control in duct flows." Journal of Aircraft, 2002; Vol 39 no. 4; pp. 616-620.

[7] Kumar,V., Alvi,F.S., “Use of high-speed microjets for active separation control in diffusers,” AIAA J., 44, pp. 273-281, 2006.

[8] Banaszuk, A., Narayanan, S. and Zhang, Y., “Adaptive control of flow separation in a planar diffuser,” *AIAA Paper* 2003-617, 2003.

[9] Vaccaro, J.C., Elimelech, Y., Chen, Y., Sahni, O., Jansen, K.E. and Amitay, M., “Experimental and numerical investigation on steady blowing flow control within a compact inlet duct,” *Intl J. Heat Fluid Fl.*, **54**, pp. 143-152, 2015.

[10] Simpson, R.L., “Turbulent boundary-layer separation,” *Annu. Rev. Fluid Mech.*, **21**, pp. 205-231, 1989.

[11] Chun, Kyung-Bin, and Sung, H. J., “Control of turbulent separated flow over a backward-facing step by local forcing,” Exp. Fluids, 21, pp. 417-426, 1996.

[12] Yoshioka, S., Obi, S., and Masuda, S., “Organized vortex motion in periodically perturbed turbulent separated flow over a backward-facing step,” Intl J. Heat Fluid Fl., 22, pp. 301-307, 2001.

[13] Vukasinovic, B., Rusak, Z., and Glezer, A., “Dissipative Small-scale Actuation of a Turbulent Shear Layer,” *J. Fluid Mechanics*, **656**, pp. 51-81, 2010.

[14] Marusic, I. and Perry, A.E., “A wake model for the turbulent structure of boundary layers. Part 2. Further experimental support,” *J. Fluid Mechanics*. **298**, pp. 389 – 407, 1995.

[15] Elsberry, K., Loeffler, J., Zhou, M.D., and Wygnanski, I., “An experimental study of a boundary layer that is maintained on the verge of separation,” *J. Fluid Mechanics*. **423**, pp 227-261, 2000.

[16] Schatzman, D.M., and Thomas, F.O., “An experimental investigation of an unsteady adverse pressure gradient turbulent boundary layer: embedded shear layer scaling,” *J. Fluids Mechanics*, **815**, pp. 592-642, 2017.

[17] Peterson, C.J., Vukasinovic, B., and Glezer. A., “Characterization of controlled flow separation,” *AIAA Paper 2018-1282*, 2018.

[18] Johnston, J.P., Nishi, M., J.K., “Vortex Generator Jets – Means for Flow Separation Control,” *AIAA Journal*, Vol 28 No. 6, pp. 989-994, 1990.

[19] Ostermann, F., Woszidlo, R., Nayeri, C. Navid, and Paschereit, C. Oliver., “The interaction between a spatially oscillating jet emitted by a fluidic oscillator and a cross-flow,” *J. Fluid Mechanics*. **863**, pp 215-241, 2019.

[20] Ostermann, F., Woszidlo, R., Nayeri, C. Navid, and Paschereit, C. Oliver., “Interaction between a Jet emitted by a Fluidic Oscillator and a Crossflow at a Skew Angle,” *AIAA Paper 2019-0887*, 2019.

[21] Otto, C., Tewes, P., Little, J. C., and Woszidlo, R., “Comparison of Fluidic Oscillators and Steady Jets for Separation Control on a Wall-Mounted Hump,” *AIAA Paper 2018-1281*, 2018.

[22] Otto, C., Tewes, P., Little, J. C., and Woszidlo, R., “Comparison of Various Fluidic Oscillators for Separation Control on a Wall-Mounted Hump,” *AIAA Paper 2019-0884*, 2019.

[23] Woszidlo, R., Ostermann, F., Schmidt, H. “Fundamental Properties of Fluidic Oscillators for Flow Control Applications,” *AIAA Journal*. **57(3)**, 2019.

[24] Kim, S., Kim, K., “Effects of Installation Conditions of Fluidic Oscillators on Control of Flow Separation,” *AIAA Journal*, 2019.

[25] Namgyal, L., Hall, J.W., “Reynolds stress distribution and turbulence generated secondary flow in the turbulent three-dimensional wall jet,” *J. Fluid Mechanics*, **800**, pp. 613-644, 2016.

[26] Matsuda, H., Iida, S., Hayakawa, M., “Coherent Structures in a Three-Dimensional Wall Jet,”, *Trans. Of the ASME*, Vol 112, 1990.

[27] Pauley, W., Eaton, J.K., “Experimental Study of the Development of Longitudinal Vortex Pairs Embedded in a Turbulent Boundary Layer,” *AIAA Journal*, Vol 26, pp. 816-823, 1988.

[28] Peterson, C.J., Vukasinovic, B., and Glezer. A., “Control of a Closed Separation Domain in Adverse Pressure Gradient Over a Curved Surface,” AIAA Paper 2019-1900, 2019.